2013

Cross sections for the $\vec{\gamma}p \to K^{*}+\Lambda$ and $\vec{\gamma}p \to K^{*}+\Sigma^{0}$ reactions measured at CLAS

K.P. Adhikari
Old Dominion University

M. J. Amaryan
Old Dominion University

C. E. Hyde
Old Dominion University

S. Koirala
Old Dominion University

M. Mayer
Old Dominion University

See next page for additional authors

Cross sections for the $\gamma p \to K^{*+}\Lambda$ and $\gamma p \to K^{*+}\Sigma^0$ reactions measured at CLAS

W. Tang,[1] K. Hicks,[1] D. Keller,[1,*] S. H. Kim,[40,†] H. C. Kim,[40] K. P. Adhikari,[28] M. Aghasyan,[18] M. J. Amaryan,[28] M. D. Anderson,[36] S. Anefalos Pereira,[18] N. A. Baltzell,[2,33] M. Battaglieri,[19] I. Bedlinskiy,[22] A. S. Biselli,[6,12] J. Bono,[13] S. Boiarinov,[34] W. J. Briscoe,[15] V. D. Burkert,[34] D. S. Carman,[34] A. Celentano,[19] S. Chandavar,[1] G. Charles,[8] P. L. Cole,[16,34] P. Collins,[7] M. Contalbrigo,[17] O. Cortes,[16] V. Crede,[14] A. D'Angelo,[20,31] N. Dashyan,[39] R. De Vita,[19] E. De Sanctis,[18] A. Deur,[34] C. Djalali,[33] D. Doughty,[9,34] R. Dupre,[21] A. El Alaoui,[2] L. El Fassi,[2] P. Eugenio,[14] G. Fedotov,[32,33] S. Fegan,[36,‡] J. A. Fleming,[11] M. Y. Gabrielyan,[13] N. Gevorgyan,[39] G. P. Gilfoyle,[30] K. L. Giovanetti,[23] F. X. Girod,[8,34] W. Gohn,[10] E. Golovatch,[32] R. W. Gothe,[33] K. A. Griffioen,[38] M. Guidal,[21] L. Guo,[13,34] K. Hafidi,[2] H. Hakobyan,[35,39] C. Hanretty,[37] N. Harrison,[10] D. Heddle,[9,34] D. Ho,[6] M. Holtrop,[26] C. E. Hyde,[28] Y. Ilieva,[15,33] D. G. Ireland,[36] B. S. Ishkhanov,[32] E. L. Isupov,[32] H. S. Jo,[21] K. Joo,[10] M. Khandaker,[27] P. Khetarpal,[13] A. Kim,[24] W. Kim,[24] F. J. Klein,[7] S. Koirala,[28] A. Kubarovsky,[29,32,§] V. Kubarovsky,[29,34] S. V. Kuleshov,[22,35] K. Livingston,[36] H. Y. Lu,[6] I. J. D. MacGregor,[36] Y. Mao,[33] N. Markov,[10] D. Martinez,[16] M. Mayer,[28] B. McKinnon,[36] C. A. Meyer,[6] V. Mokeev,[32,34,‖] H. Moutarde,[8] E. Munevar,[34] C. Munoz Camacho,[21] P. Nadel-Turonski,[34] C. S. Nepali,[28] S. Niccolai,[21] G. Niculescu,[23] I. Niculescu,[23] M. Osipenko,[19] A. I. Ostrovidov,[14] L. L. Pappalardo,[17] R. Paremuzyan,[39,¶] K. Park,[24,34] S. Park,[14] E. Pasyuk,[3,34] E. Phelps,[33] J. J. Phillips,[36] S. Pisano,[18] O. Pogorelko,[22] S. Pozdniakov,[22] J. W. Price,[4] S. Procureur,[8] Y. Prok,[9,37,**] D. Protopopescu,[36] A. J. R. Puckett,[34] B. A. Raue,[13,34] M. Ripani,[19] D. Rimal,[13] B. G. Ritchie,[3] G. Rosner,[36] P. Rossi,[18] F. Sabatié,[8] M. S. Saini,[14] C. Salgado,[27] D. Schott,[15] R. A. Schumacher,[6] H. Seraydaryan,[28] Y. G. Sharabian,[34] G. D. Smith,[36] D. I. Sober,[7] D. Sokhan,[36] S. S. Stepanyan,[24] S. Stepanyan,[34] P. Stoler,[29] I. I. Strakovsky,[15] S. Strauch,[15,33] C. E. Taylor,[16] Ye Tian,[33] S. Tkachenko,[37] B. Torayev,[28] M. Ungaro,[10,29,34] B. Vernarsky,[6] A. V. Vlassov,[22] H. Voskanyan,[39] E. Voutier,[25] N. K. Walford,[7] D. P. Watts,[11] L. B. Weinstein,[28] D. P. Weygand,[34] M. H. Wood,[5,33] N. Zachariou,[33] L. Zana,[26] J. Zhang,[34] Z. W. Zhao,[37] and I. Zonta[20,††]

(CLAS Collaboration)

[1]*Ohio University, Athens, Ohio 45701, USA*
[2]*Argonne National Laboratory, Argonne, Illinois 60439, USA*
[3]*Arizona State University, Tempe, Arizona 85287-1504, USA*
[4]*California State University, Dominguez Hills, Carson, California 90747, USA*
[5]*Canisius College, Buffalo, New York, USA*
[6]*Carnegie Mellon University, Pittsburgh, Pennsylvania 15213, USA*
[7]*Catholic University of America, Washington, DC 20064, USA*
[8]*CEA, Centre de Saclay, Irfu/Service de Physique Nucléaire, 91191 Gif-sur-Yvette, France*
[9]*Christopher Newport University, Newport News, Virginia 23606, USA*
[10]*University of Connecticut, Storrs, Connecticut 06269, USA*
[11]*Edinburgh University, Edinburgh EH9 3JZ, United Kingdom*
[12]*Fairfield University, Fairfield, Connecticut 06824, USA*
[13]*Florida International University, Miami, Florida 33199, USA*
[14]*Florida State University, Tallahassee, Florida 32306, USA*
[15]*The George Washington University, Washington, DC 20052, USA*
[16]*Idaho State University, Pocatello, Idaho 83209, USA*
[17]*INFN, Sezione di Ferrara, 44100 Ferrara, Italy*
[18]*INFN, Laboratori Nazionali di Frascati, 00044 Frascati, Italy*
[19]*INFN, Sezione di Genova, 16146 Genova, Italy*
[20]*INFN, Sezione di Roma Tor Vergata, 00133 Rome, Italy*
[21]*Institut de Physique Nucléaire Orsay, Orsay, France*
[22]*Institute of Theoretical and Experimental Physics, Moscow, 117259, Russia*
[23]*James Madison University, Harrisonburg, Virginia 22807, USA*
[24]*Kyungpook National University, Daegu 702-701, Republic of Korea*
[25]*LPSC, Universite Joseph Fourier, CNRS/IN2P3, INPG, Grenoble, France*
[26]*University of New Hampshire, Durham, New Hampshire 03824-3568, USA*
[27]*Norfolk State University, Norfolk, Virginia 23504, USA*
[28]*Old Dominion University, Norfolk, Virginia 23529, USA*
[29]*Rensselaer Polytechnic Institute, Troy, New York 12180-3590, USA*
[30]*University of Richmond, Richmond, Virginia 23173, USA*
[31]*Universita' di Roma Tor Vergata, 00133 Rome, Italy*
[32]*Skobeltsyn Nuclear Physics Institute, 119899 Moscow, Russia*
[33]*University of South Carolina, Columbia, South Carolina 29208, USA*
[34]*Thomas Jefferson National Accelerator Facility, Newport News, Virginia 23606, USA*
[35]*Universidad Técnica Federico Santa María, Casilla 110-V Valparaíso, Chile*
[36]*University of Glasgow, Glasgow G12 8QQ, United Kingdom*

[37] *University of Virginia, Charlottesville, Virginia 22901, USA*
[38] *College of William and Mary, Williamsburg, Virginia 23187-8795, USA*
[39] *Yerevan Physics Institute, 375036 Yerevan, Armenia*
[40] *Inha University, Incheon 402-751, Republic of Korea*
(Received 11 March 2013; revised manuscript received 18 May 2013; published 19 June 2013)

The first high-statistics cross sections for the reactions $\gamma p \to K^{*+}\Lambda$ and $\gamma p \to K^{*+}\Sigma^0$ were measured using the CLAS detector at photon energies between threshold and 3.9 GeV at the Thomas Jefferson National Accelerator Facility. Differential cross sections are presented over the full range of the center-of-mass angles, and then fitted to Legendre polynomials to extract the total cross section. Results for the $K^{*+}\Lambda$ final state are compared with two different calculations in an isobar and a Regge model, respectively. Theoretical calculations significantly underestimate the $K^{*+}\Lambda$ total cross sections between 2.1 and 2.6 GeV, but are in better agreement with present data at higher photon energies.

DOI: 10.1103/PhysRevC.87.065204 PACS number(s): 13.60.Le, 13.60.Rj, 14.20.Jn, 14.40.Df

I. INTRODUCTION

One motivation for the study of K^* photoproduction is to investigate the role of the $K_0^*(800)$ meson (also called the κ) through t-channel exchange. The κ is expected to be in the same scalar meson nonet as the $f_0(500)$ meson (also called the σ). Neither of these mesons have been directly observed because of their large widths, which are nearly as big as their respective masses. Such a large width is expected for scalar mesons, which have quantum numbers $J^{PC} = 0^{++}$. In many quark models, there is virtually no angular momentum barrier to prevent these mesons from falling apart into two mesons, such as $\sigma \to \pi\pi$ or $\kappa \to K\pi$. Because the σ and κ mesons cannot be observed directly, indirect production mechanisms provide better evidence of their existence.

The σ meson is rather well established [1] as a $\pi\pi$ resonance, which is an important component of models of the nucleon-nucleon (NN) interaction such as the Bonn potential [2]. The κ meson, however, is less easily established due to its strange quark content. Data for hyperon-nucleon (YN) interactions are sparse and hence models have a range of parameter space that may or may not include κ exchange. Perhaps the best current evidence for the κ is from the decay angular distributions of the D-meson into $K\pi\pi$ final states [3].

Here, in photoproduction of the K^{*+}, the κ^+ enters into the t-channel exchange diagrams [4]. The κ cannot contribute to kaon photoproduction because the photon cannot couple to the K-κ vertex due to G-parity conservation. Theoretical calculations have been done [4] showing the effect of the κ on photoproduction of K^{*+} and K^{*0} final states. Several years ago, two reports of K^{*0} photoproduction were published [5,6] but only preliminary results on K^{*+} were available [7].

We present the first results of $K^{*+}\Lambda$ and $K^{*+}\Sigma^0$ photoproduction with high statistics. Together, the K^{*+} and K^{*0} photoproduction results could put significant constraints on the role of the κ meson in t-channel exchange. Here, for the first time, we make the ratio of total cross sections for the reactions $\gamma p \to K^{*+}\Lambda$ and $\gamma p \to K^{*0}\Sigma^+$ and compare with the same ratio calculated from a theoretical model for large and small contributions from κ exchange. Other evidence for the κ comes from recently published data on the linear beam asymmetry in photoproduction of the $\vec{\gamma} p \to K^{*0}\Sigma^+$ reaction [8] which shows a significant positive value at forward K^* angles that is the signature of κ exchange [4].

A secondary motivation for this study is to understand if theoretical models using Regge trajectories plus known baryon resonances can explain the K^{*+} photoproduction data. If not, then there may be higher-mass baryon resonances that could couple strongly to K^*Y decay. In a classic paper on the quark model, Capstick and Roberts calculated [9] many nucleon resonances that were predicted, but not observed in existing partial wave analyses of pion-nucleon scattering. They also observed that some of the higher-mass resonances may couple weakly to pion decay channels and more strongly to KY and K^*Y decays. Indeed, studies of KY photoproduction [10] have shown that hadronic model calculations cannot explain the data without the addition of a new nucleon resonance near 1.9 GeV. We can look for other missing resonance states at higher mass, such as those identified in the Bonn-Gatchina analysis [11], by comparing K^* photoproduction data to model calculations.

This paper is organized into the following sections. First, the experiment is described. Next, the data analysis is presented in some detail. Then we compare the results with theoretical calculations. Finally, we discuss the significance of the comparison and provide some conclusions.

II. EXPERIMENTAL SETUP

The data used in this analysis are from part of the g11a experiment, which was taken from May 17 to July 29, 2004,

*Present address: University of Virginia, Charlottesville, Virginia 22901, USA.
†Present address: Osaka University, 567-0047 Ibarakishi, Japan.
‡Present address: INFN, Sezione di Genova, 16146 Genova, Italy.
§Present address: University of Connecticut, Storrs, Connecticut 06269, USA.
‖Present address: Skobeltsyn Nuclear Physics Institute, 119899 Moscow, Russia.
¶Present address: Institut de Physique Nucléaire ORSAY, Orsay, France.
**Present address: Old Dominion University, Norfolk, Virginia 23529, USA.
††Present address: Universita' di Roma Tor Vergata, 00133 Rome, Italy.

using the CEBAF Large Acceptance Spectrometer (CLAS) located in Hall-B at the Thomas Jefferson National Accelerator Facility (TJNAF) in Newport News, Virginia. Real photons were produced by bremsstrahlung from a 4.0186 GeV electron beam incident on a 1×10^{-4} radiation length gold foil. The electron beam was delivered by the Continuous Electron Beam Accelerator Facility (CEBAF). The Hall-B Tagging System [12] was used to determine the photon energies by measuring the energies of the recoil electrons using a dipole magnetic field and a scintillator hodoscope. The associated photon energies were then calculated by the difference between the incident electron energies and the recoil electron energies with an energy resolution of about 2–3 MeV. The Hall-B Tagging System tags photons in the range from 20% to 95% of the incident electron energy.

A liquid hydrogen target was used in the g11a experiment. The target was contained in a cylindrical Kapton chamber of 2 cm radius and 40 cm length. The target density was determined by the temperature and pressure, which were monitored once per hour during the g11a experiment running.

The CLAS apparatus was used to detect particles generated from the interaction of the incident photons with the target. The CLAS detector was able to track charged particles that have momenta larger than $\sim$0.2 GeV/c, and the detection area covered polar angles from 8° to 142° and 80% of the azimuthal region. It was composed of several subsystems, arranged with a sixfold azimuthal symmetry. A plastic scintillator Start Counter, placed just outside of the target, was used to measure the vertex time of particles in coincidence with the incoming photon. The Start Counter was made of 24 scintillator strips with a time resolution of $\sim$350 ps [13]. The superconducting coils of the CLAS detector generated a toroidal magnetic field that bent the path of outgoing charged particles. Those particles traveled through three regions of drift chambers [14] that measured the curved paths to give the particle momenta with a typical resolution of $\sim$1.0%. For the g11a experiment, the current in the superconducting coils was set at 1920 A, which gave a maximum magnetic field of $\sim$1.8 T. The time of flight (TOF) system was located beyond the outermost drift chambers at a radius of $\sim$4 m from the target and was used to measure the time and position of each charged particle that hit the TOF scintillators. The TOF information, along with the particle momentum, was used for the particle identification in the analysis. The time resolution of the TOF system was about 80 ps to 160 ps, depending on the length of the scintillators [15]. A more detailed description of the CLAS detector is given in Ref. [16].

The event trigger for the g11a experiment required that at least two tracks were detected in different sectors of CLAS. Once the event satisfied this condition, it was written to tape for future analysis. The data acquisition system for the g11a experiment was able to run at $\sim$5 kHz with a typical livetime of 90%.

III. DATA ANALYSIS

As one of the largest photoproduction datasets at CLAS, the g11a experiment has $\sim$20 billion triggers. The calibration of each CLAS subsystem followed the same procedures as described in Ref. [17]. Additional details can be found in Ref. [18].

TABLE I. Some physical properties of the K^{*+}, Λ, and Σ^0 [1].

	K^{*+}	Λ	Σ^0
Mass(GeV/c^2)	0.89166	1.11568	1.19264
Decay products	$K^0\pi^+$, $K^+\pi^0$	$p\pi^-$, $n\pi^0$	$\Lambda\gamma$
Branching fraction	66.7%, 33.3%	63.9%, 35.8%	100%

A. Channels of interest

Because the K^{*+} is an unstable particle, it will quickly decay to $K\pi$ (see Table I) by the strong interaction. By applying energy and momentum conservation, the K^{*+} momentum is reconstructed from its decay particles, $K^0\pi^+$. The K^0 is a mixture of 50% K_S and 50% K_L, but only the K_S decay is detected by the CLAS detector. The K^0 is reconstructed from the K_S decay to $\pi^+\pi^-$ with a decay branching fraction of 69.2%. The same branching fractions are reproduced by the Monte Carlo detector simulations (see Sec. III F), and hence are implicit in the detector acceptance values.

To summarize, we report on the differential and total cross sections of the photoproduction channel(s):

$$\gamma p \rightarrow K^{*+}\Lambda(\Sigma^0) \tag{1}$$

followed by

$$K^{*+} \rightarrow K^0\pi^+ \tag{2}$$

and

$$K_S \rightarrow \pi^+\pi^- . \tag{3}$$

The K^{*+} and K_S are reconstructed directly from their decay products, while the Λ and Σ^0 are reconstructed using the missing mass technique.

B. Particle identification

The time of flight (TOF) difference method was used to identify events with three pions (two positive and one negative charge) in the final state. Explicitly,

$$\Delta\text{tof} = \text{tof}_{\text{mea}} - \text{tof}_{\text{cal}}, \tag{4}$$

where tof_{mea} is the measured TOF of the particle and tof_{cal} is the calculated TOF with the measured momentum p and the mass of a pion. In more detail,

$$\text{tof}_{\text{mea}} = t_{\text{tof}} - t_{\text{st}}, \tag{5}$$

where t_{tof} is the time when the particle hits the TOF scintillators and t_{st} is the time when the photon hits the target. This information is determined by the CLAS Start Counter. In comparison, tof_{cal} is given by

$$\text{tof}_{\text{cal}} = \frac{L}{c} \cdot \frac{1}{\beta}, \tag{6}$$

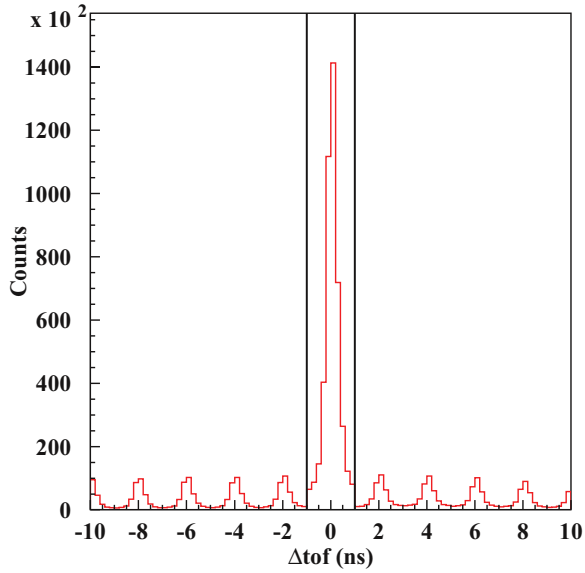

FIG. 1. (Color online) The TOF difference spectrum for pions. The two straight lines show the cut limits for selecting pions in a time window of ±1.0 ns.

where

$$\beta = \frac{p}{\sqrt{p^2 + m^2}}. \tag{7}$$

Thus

$$\mathrm{tof}_{\mathrm{cal}} = \frac{L}{c} \cdot \sqrt{1 + \frac{m^2}{p^2}}, \tag{8}$$

where L is the path length from the target to the TOF scintillators, c is the speed of light, p is the particle's momentum, and m is the mass of a pion. The pion candidates are required to have $|\Delta\mathrm{tof}| < 1.0$ ns. Figure 1 shows the TOF difference spectrum. The solid lines define the region of the cut, the small peaks on the both side of the cuts are due to photons coming from other beam bunches, showing evidence of the ∼2 ns beam bunch structure of CEBAF.

C. Photon selection

After applying the $|\Delta\mathrm{tof}| < 1.0$ ns cut, particles that came from different RF beam buckets were removed naturally. Of the photons measured by the photon tagger, we want those that come within 1.0 ns of the particle vertex time, which are called "good" photons. However, there might still be more than one "good" photon in each event. To select the correct photon, all "good" photons were scanned to find the one that gave the three-pion missing mass closest to the known mass of the $\Lambda(\Sigma^0)$, where

$$MM(\pi^+\pi^-\pi^+) = \sqrt{\left(E_\gamma + m_p - \sum E_\pi\right)^2 - \left(\vec{p}_\gamma - \sum \vec{p}_\pi\right)^2} \tag{9}$$

is the missing mass summed over all three pions in the event, while E_γ and $\vec{p}_\gamma$ are the energy and momentum vector of the photon. The two-pion missing mass is similarly defined.

D. Cuts applied

Several cuts were applied to the data to reduce the background and to remove events below threshold for the reaction of interest. In general, the strategy is to use geometric and kinematic constraints to eliminate backgrounds while ensuring that the signal remains robust. The efficiency of various cuts was tested with Monte Carlo simulations (see Sec. III G).

The geometric and kinematic constraints used here are listed below:

(i) Fiducial cuts were applied to remove events that were detected in regions of the CLAS detector where the calibration of the detector is not well understood.

(ii) A cut on the vertex position along the beam axis (the z-axis) to be within the target position was applied. All pions were required to be generated from the same vertex position within the experimental position uncertainty.

(iii) The missing mass from the K^0 was required to satisfy the relation $MM(\pi^+\pi^-) > 1.0$ GeV/c^2 to include all hyperon mass peaks, for pion pairs with an invariant mass inside the K^0 mass window (see next section). Similarly, the missing mass from the K^{*+} was required to be greater than the nucleon mass, $MM(\pi^+\pi^-\pi^+) > 1.0$ GeV/c^2. After this step, the $K^{*+}\Lambda$ and $K^{*+}\Sigma^0$ reaction channels were treated differently, since different backgrounds are present for each final state. For instance, the large background from

$$\gamma p \to K^0\Sigma^{*+}(1385) \tag{10}$$

present for the $K^{*+}\Lambda$ reaction channel makes the extraction of $K^{*+}\Lambda$ yields by simply fitting the Λ peak impossible. On the other hand, there are only very small portions of the $\Sigma^{*+}(1385)$ that contribute to the $K^{*+}\Sigma^0$ background, which can be easily removed based on Monte Carlo studies (see following section). Thus we could fit directly the Σ^0 peak in the three-pion missing mass for $K^{*+}\Sigma^0$ channel, whereas a different approach (given below) is necessary to extract the $K^{*+}\Lambda$ yield separately from background due to $K^0\Sigma^{*+}(1385)$ production. The following lists the extra cuts applied for each reaction channel.

(iv) For the $K^{*+}\Lambda$ analysis, a cut was placed on the Λ peak in the three-pion missing mass: 1.08 GeV/$c^2 < MM(\pi^+\pi^-\pi^+) < 1.15$ GeV/c^2. This ensures that a Λ was present in the final state.

(v) For the $K^{*+}\Sigma^0$ analysis, a cut was placed on the K^{*+} peak of the three-pion invariant mass: 0.812 GeV/$c^2 < M(\pi^+\pi^-\pi^+) < 0.972$ GeV/c^2. This ensures that a K^{*+} was produced.

E. Sideband subtraction

Because reactions other than K^* photoproduction are present, background is still mixed in with the channels of interest. Figure 2 shows the two-pion invariant mass plot after the first three cuts in the previous section, integrated over all photon energies. A clear peak centered near 0.497 GeV sits on

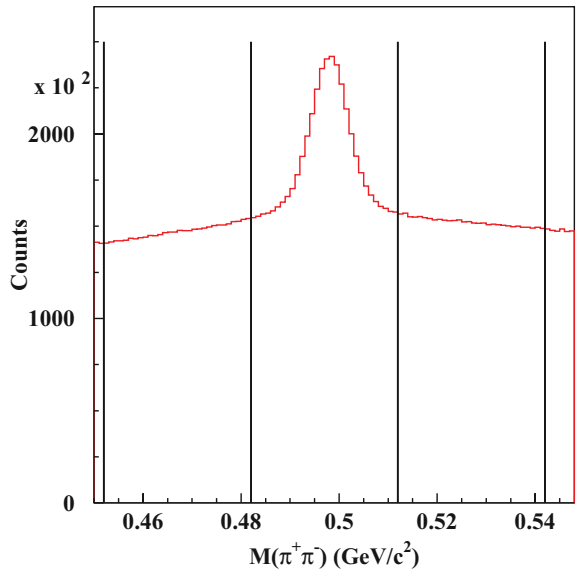

FIG. 2. (Color online) The reconstructed two-pion invariant mass showing the K_S distribution. The vertical lines define the bands for the SSM, as explained in the text.

top of a smooth background. The invariant mass is calculated using the momentum vector of one π^+ in the event, along with the π^- momentum. Since there are two π^+s, both $\pi^+\pi^-$ pairs are tested, but typically only one combination will satisfy all kinematic constraints. To avoid double-counting, in rare cases where both π^+ satisfy all constraints, this combinatoric background is removed, for both data analysis and Monte Carlo acceptances.

To reduce the background, a sideband subtraction method (SSM) was applied. The concept of the SSM is to assume that the background in the signal region can be approximated by a combination of the left and the right regions, which are adjacent to the signal region. In our analysis, the two-pion mass of the K_S is used as the criteria to select the signal and sideband regions. Figure 2 shows the regions used in our analysis. The middle band is the signal region, centered at the mass of K^0 with a width of 0.03 GeV. The other two bands, with the same band sizes, are the combinatorial background.

Figure 3 shows the sideband subtraction applied to the reconstructed three-pion invariant mass and to the three-pion missing mass. The SSM reduces the background, giving cleaner signal peaks. Note that there is some remaining structure in Figs. 3(a) and 3(c) of the three-pion missing mass. This is due to a small leakage of the gaussian tail of the K^0 signal into the two background regions. We also see the same amount of leakage in the Monte Carlo sideband regions, which is used to calculate the detector acceptance. The net effect of this small leakage is canceled out (to first order) in the cross section results. The systematic error due to the leakage will be described in a later section.

F. Peak fitting

After applying the SSM to each $M(\pi^+\pi^+\pi^-)$ invariant mass plot, corresponding to different incident photon energy and different K^{*+} production angle ranges, the K^{*+} peak becomes clearer, but it is still not free of background. The main contribution to the background comes from the reaction channel $\gamma p \to K^0\Sigma^{*+}(1385)$, which passed through all the cuts. In

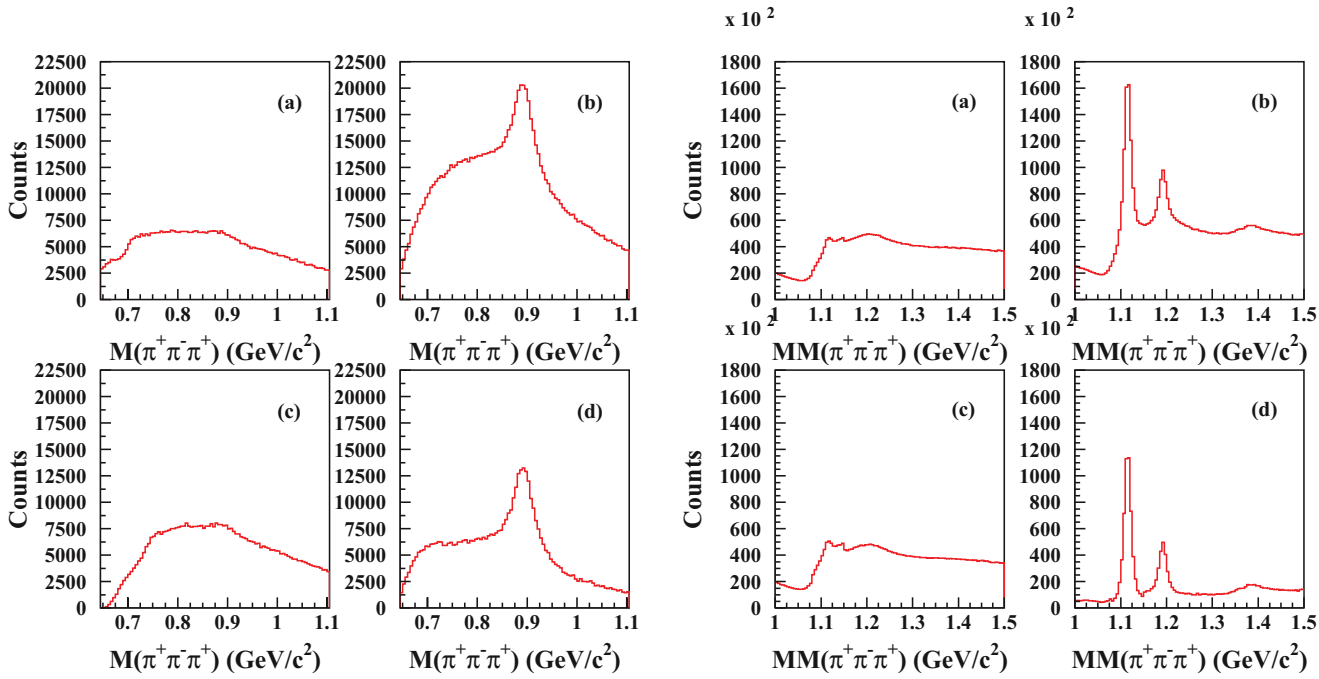

FIG. 3. (Color online) Three-pion invariant mass (left) and the three-pion missing mass (right). The four plots in each group correspond to: (a) the left band, (b) the middle band before the SSM, (c) the right band, and (d) the middle band after the SSM. The peak in the three-pion mass is the K^{*+} and the peaks in the three-pion missing mass are the Λ and Σ^0. All plots are integrated over all incident photon energies.

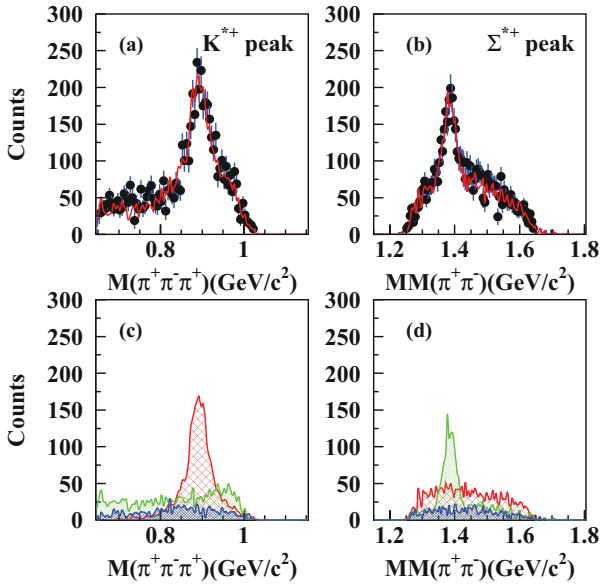

FIG. 4. (Color online) Example of the template fitting. (a) and (b): the solid dots are from the data, while the curve is from the fitting, which contains contributions from the $K^{*+}\Lambda$, $K^0\Sigma^{*+}$ and $K^0\pi^+\Lambda$ channels, shown individually by (c) and (d) at the bottom in large red diagonal cross, forward green diagonal, and small blue diagonal cross histograms, respectively.

addition, the three-body phase space reaction $\gamma p \to K^0\pi^+\Lambda$ is also present, and will contribute to the background as well.

In order to extract the correct K^{*+} peak yield, instead of fitting the K^{*+} peaks directly with a Breit-Wigner plus background functions, we applied a template fit. The precondition for this template fitting is that we assume there is negligible interference between the $K^{*+}\Lambda$ and $K^0\Sigma^{*+}(1385)$ channels; in other words, we assume that the $K^{*+}\Lambda$ and $K^0\Sigma^{*+}(1385)$ add incoherently. If we remove all other sources of background, then the K^{*+} mass plot should have background only from the $\Sigma^{*+}(1385)$ peak. Similarly, the background in the $\Sigma^{*+}(1385)$ plot comes only from events in the K^{*+} peak. Because the three-body $K^0\pi^+\Lambda$ channel is also a possible background, we assume it will add incoherently as well in both mass projections.

To justify these assumptions, we explored the effect of various levels of interference between these two final states in the simulations. The result is that the template fits correctly reproduced the generated events to within a 5% uncertainty for assumptions of maximal constructive or destructive interference.

Figure 4 shows an example of the template fitting, where the solid dots with error bars are from the data, while the curve is from the fit, which contains contributions from both the $K^{*+}\Lambda$, $K^0\Sigma^{*+}$ and $K^0\pi^+\Lambda$ channels. The K^{*+} peak is seen in the left plots and the Σ^{*+} peak is seen in the right plots. The template shape for each contribution comes from the simulation for that channel, and the magnitude of each channel is a free parameter to optimize the fit, with the result for each component of the fit shown in the bottom plots of Fig. 4. Both mass projections of Fig. 4 are fit simultaneously to minimize the overall χ^2.

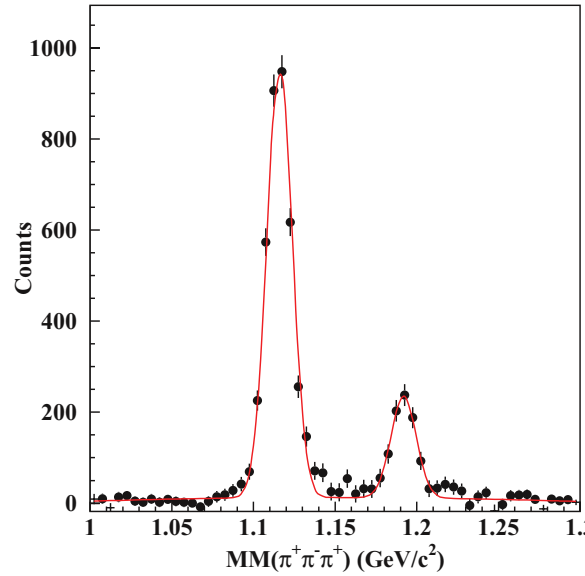

FIG. 5. (Color online) Example of two Gaussians plus a second order polynomial fit to the reconstructed Λ and Σ^0 missing mass peaks.

For the $K^{*+}\Sigma^0$ reaction, the counts from the Σ^0 were extracted by using a Gaussian fit, then the yields were corrected bin by bin based on a Monte Carlo study of how much $K^0\Sigma^{*+}(1385)$ leakage there is to the $K^{*+}\Sigma^0$ reaction channel. The correction was studied and found to be less than 0.1%, which was included in our cross section calculation. Figure 5 shows an example of the fitting. There are two peaks in the three-pion missing mass plot, one corresponding to the Λ and the other to the Σ^0. The fitting function used two Gaussians plus a second order polynomial, for the Λ peak, Σ^0 peak and background, respectively.

G. Detector acceptance

A computational simulation package, the CLAS GEANT Simulation (GSIM), was used for the Monte Carlo modeling of the detector acceptance. GSIM is based on the CERN GEANT simulation code with the CLAS detector geometry. Thirty million $\gamma p \to K^{*+}\Lambda$ (Σ^0) events were randomly generated, with all possible decay channels of the final state particles (K^{*+}, Λ, Σ^0, ...). The Monte Carlo files were generated with a Bremsstrahlung photon energy distribution and a tunable angular distribution that best fit the K^* data. The energy bin size was 0.1 GeV and the total cross section was assumed constant across the bin. This assumption is reasonable based on the slowly-varying total cross sections shown below. Because the simulations have a better resolution than the real CLAS data, the output from GSIM are put through a software program to smear the particle momentum, timing, *etc.* to better match the real data.

An extensive study of the g11a trigger [17] showed a small inefficiency for the experimental trigger. To account for the trigger inefficiency, an empirical correction was mapped into the Monte Carlo. The trigger corrections applied here is the same as used for other CLAS analyses of this same dataset [17].

The detector acceptance is calculated by

$$\epsilon = \frac{D_{\mathrm{MC}}}{G_{\mathrm{MC}}}, \tag{11}$$

where D_{MC} is the number of accepted events after processing and G_{MC} is the number of generated events.

The same software used for the experimental data was applied directly to the Monte Carlo data. Simulated events are extracted by fitting each reconstructed K^{*+} peak for a given photon energy and K^{*+} production angle. In our analysis, a nonrelativistic Breit-Wigner function

$$|\mathcal{A}_{\mathrm{non}-r\mathrm{BW}}|^2 = A\frac{\Gamma}{2\pi}\frac{1}{(E-E_R)^2+\Gamma^2/4}, \tag{12}$$

was used to extract the counts of the K^{*+} peaks for $K^{*+}\Lambda$ channel. Here, Γ is the full width at half-maximum of the resonance peak, E is the scattering energy and E_R is the center of the resonance.

As described in Sec. III D, different methods were used for the $K^{*+}\Lambda$ and $K^{*+}\Sigma^0$ channels due to the presence of Λ^* resonance contributions in the former. For the $K^{*+}\Sigma^0$ channel, where there is no kinematic overlap from hyperon states, the counts under the Σ^0 peak were fitted directly using a Gaussian function. Fitting the three-pion missing mass of the Σ^0 has less uncertainty than fitting the K^{*+} peak, since the Σ^0 peak is relatively narrow on top of a nearly flat background. This method was used for both simulated and experimental data.

IV. NORMALIZATION AND CROSS SECTION RESULTS

The differential cross sections are calculated by the formula:

$$\frac{d\sigma}{d\cos\theta^{\mathrm{c.m.}}_{K^{*+}}} = \frac{Y}{N_{\mathrm{target}}\cdot N_{g\mathrm{flux}}\cdot\varepsilon\cdot\Delta\cos\theta^{\mathrm{c.m.}}_{K^{*+}}\cdot f_{lt}}, \tag{13}$$

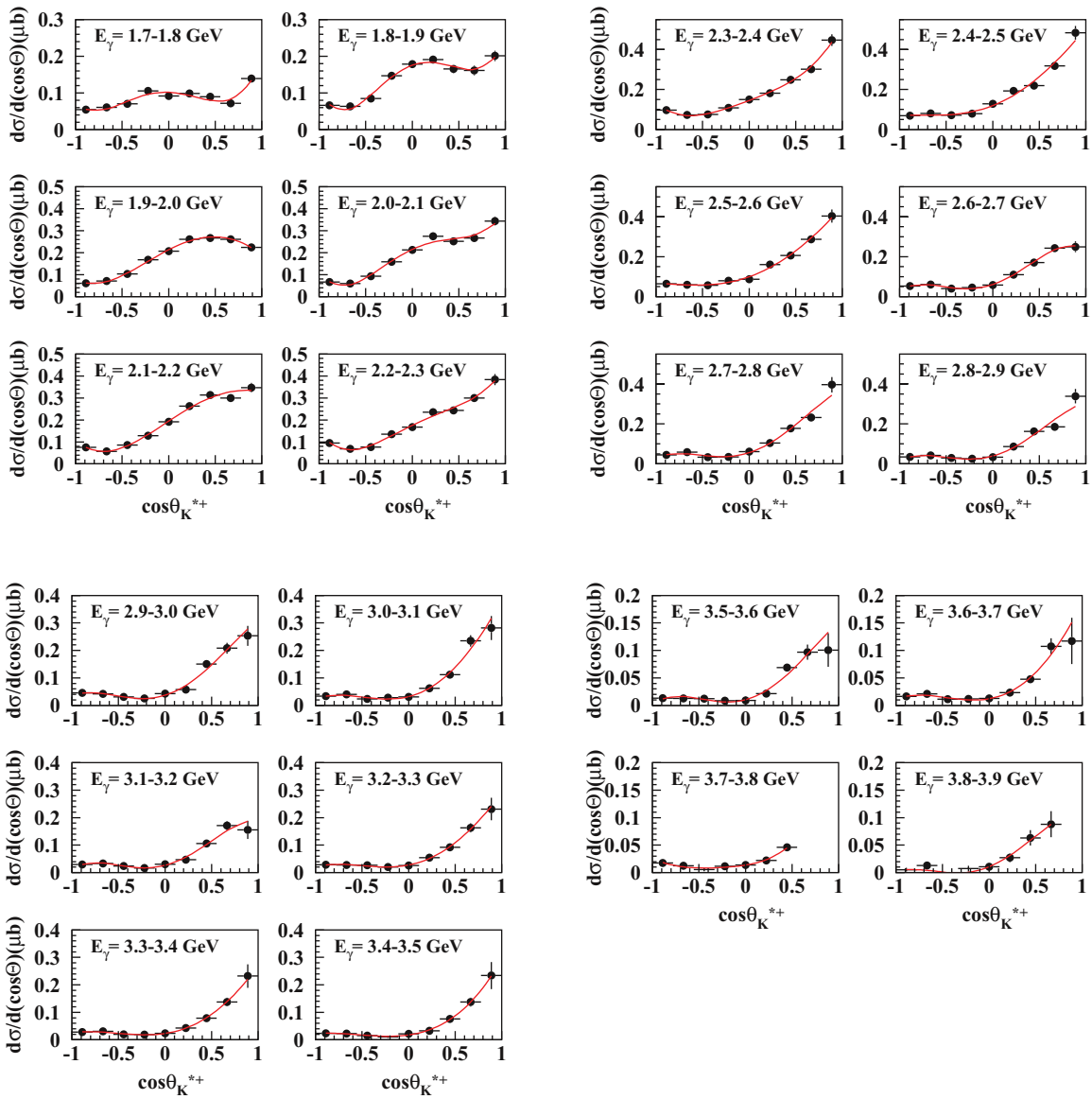

FIG. 6. (Color online) Fitting the differential cross sections for $\gamma p \to K^{*+}\Lambda$ with fourth-order Legendre polynomials. Incoming photon energies range from 1.7 to 3.9 GeV.

where $\frac{d\sigma}{d\cos\theta^{\text{c.m.}}_{K^{*+}}}$ is the differential cross section in the K^{*+} angle center-of-mass (c.m.) frame, Y is the experimental yield, N_{target} is the area density of protons in the target, $N_{g\text{flux}}$ is the incident photon beam flux, ε is the detector acceptance, $\Delta\cos\theta^{\text{c.m.}}_{K^{*+}}$ is the bin size in the K^{*+} angle in the c.m. frame, and f_{lt} is the DAQ livetime for the experiment.

The detector acceptance ε and experimental yields Y for the $K^{*+}\Lambda$ and $K^{*+}\Sigma^0$ reactions are described in the previous sections.

For each incident photon beam energy range ($\Delta E = 0.1$ GeV), nine angular regions were measured, uniformly distributed between $-1.0 < \cos\theta^{\text{c.m.}}_{K^{*+}} < 1.0$. Hence, $\Delta\cos\theta^{\text{c.m.}}_{K^{*+}}$ is $\frac{2}{9}$. The livetime f_{lt} for the g11a experiment was carefully studied as a function of beam intensity, and found to be 0.82 ± 0.01 for this measurement [19].

In our analysis, photon flux was extracted in photon energy steps of 0.05 GeV. In the final analysis, we used photon energy bins of 0.1 GeV, and the fluxes added appropriately.

The proton density N_{target} is calculated using the formula:

$$N_{\text{target}} = \frac{\rho \cdot L \cdot N_A}{A}, \tag{14}$$

where ρ, L, and A are the target density, target length and the atomic weight of hydrogen, respectively. N_A is Avogadro's number. For the g11a experiment, an unpolarized liquid hydrogen target was used. The target density ρ was measured using

$$\rho = a_1 T^2 + a_2 P + a_3, \tag{15}$$

where T, P are the target temperature and pressure (measured at the beginning of each CLAS run), while a_1, a_2, a_3

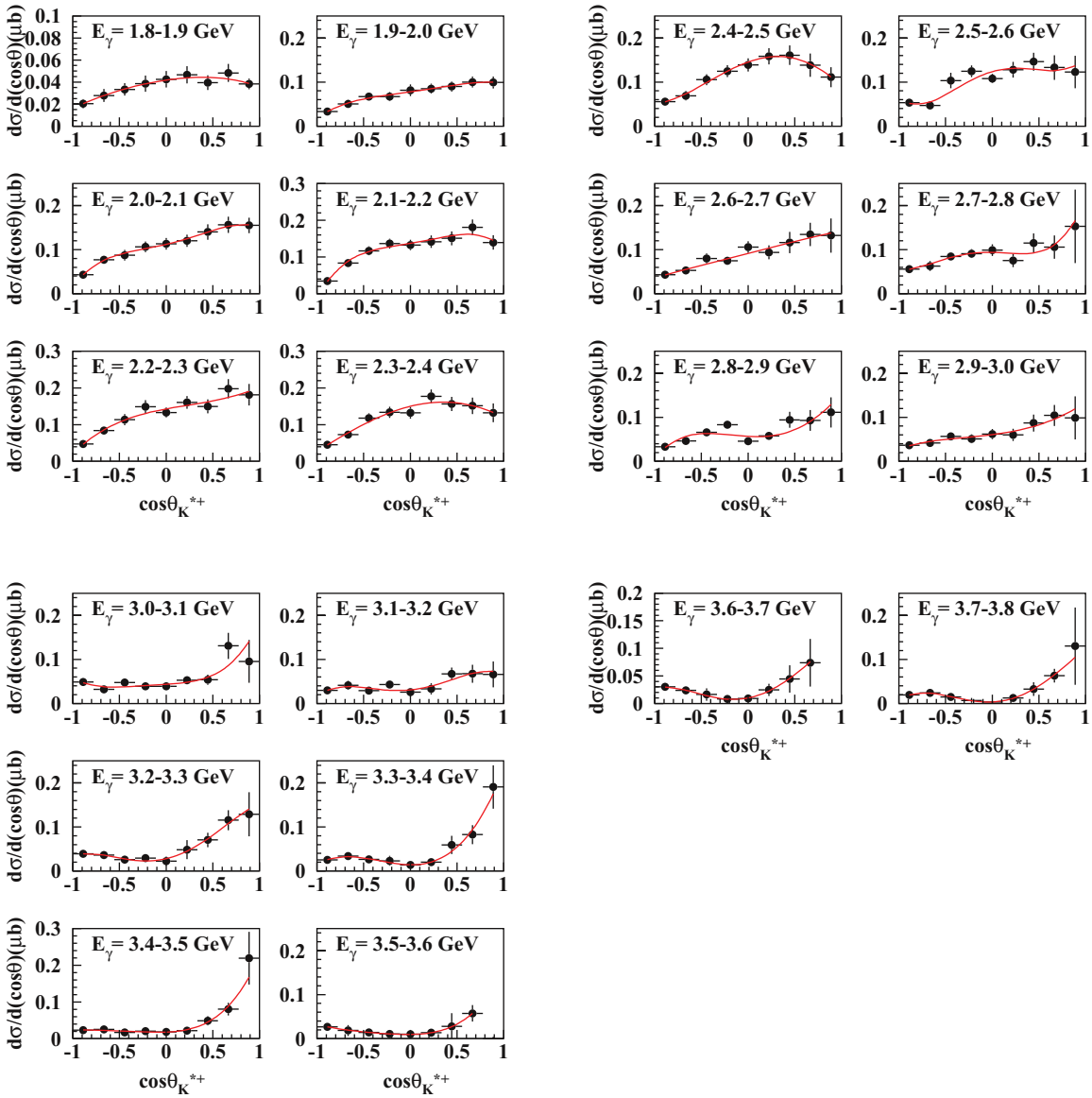

FIG. 7. (Color online) Fitting the differential cross section for $\gamma p \to K^{*+}\Sigma^0$ with fourth-order Legendre polynomials. Incoming photon energies range from 1.8 to 3.8 GeV.

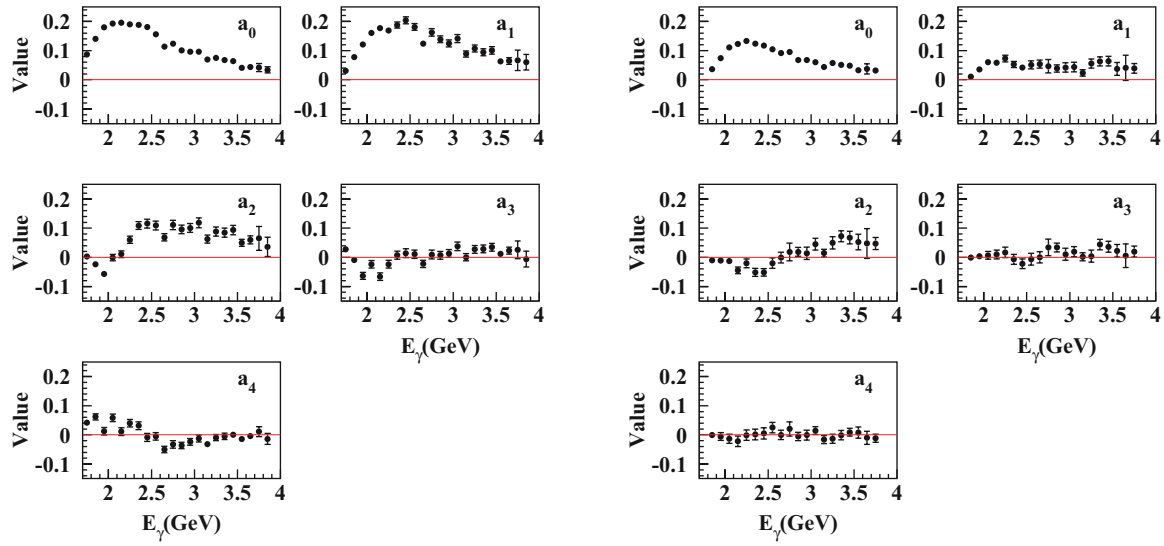

FIG. 8. (Color online) Legendre polynomial fitting parameters up to fourth order plotted versus incident photon energy E_γ for $\gamma p \to K^{*+}\Lambda$ (left) and $\gamma p \to K^{*+}\Sigma^0$ (right).

are the fitting parameters. The mean value of the target density ρ for the g11a data was obtained by taking the average [17]:

$$\overline{\rho} = \frac{1}{N_{\rm run}} \sum \rho_r = 0.07177 \text{g/cm}^3, \tag{16}$$

where $N_{\rm run}$ is the number of runs. Using the target length of 40 cm, this gives $N_{\rm target}$.

V. RESULTS

Figure 6 shows the differential cross sections for the photoproduction reaction $\gamma p \to K^{*+}\Lambda$, where there are 22 plots, for E_γ bins ranging from 1.70 to 3.90 GeV. There are nine angular measurements in each plot, uniformly distributed in $\cos\theta^{\rm c.m.}_{K^{*+}}$ between -1.0 and 1.0. In general, the $K^{*+}\Lambda$ differential cross sections shows dominantly a t-channel behavior, with an increase at forward angles. Similarly, Fig. 7 shows the differential cross sections for $\gamma p \to K^{*+}\Sigma^0$ photoproduction over the same photon energy range. Comparison with theoretical calculations are given below in Sec. V B.

The differential cross sections can be decomposed into Legendre polynomials as [10]

$$\frac{d\sigma}{d\cos\theta} = \frac{\sigma_{\rm total}}{2}\left\{1 + \sum_{i=1}^{N} a_i\, p_i(x)\right\}, \tag{17}$$

where $\sigma_{\rm total}$ is the total cross section. By fitting the differential cross sections up to fourth-order Legendre polynomials

$$f(x) = \sum_{i=0}^{4} a_i\, p_i(x), \tag{18}$$

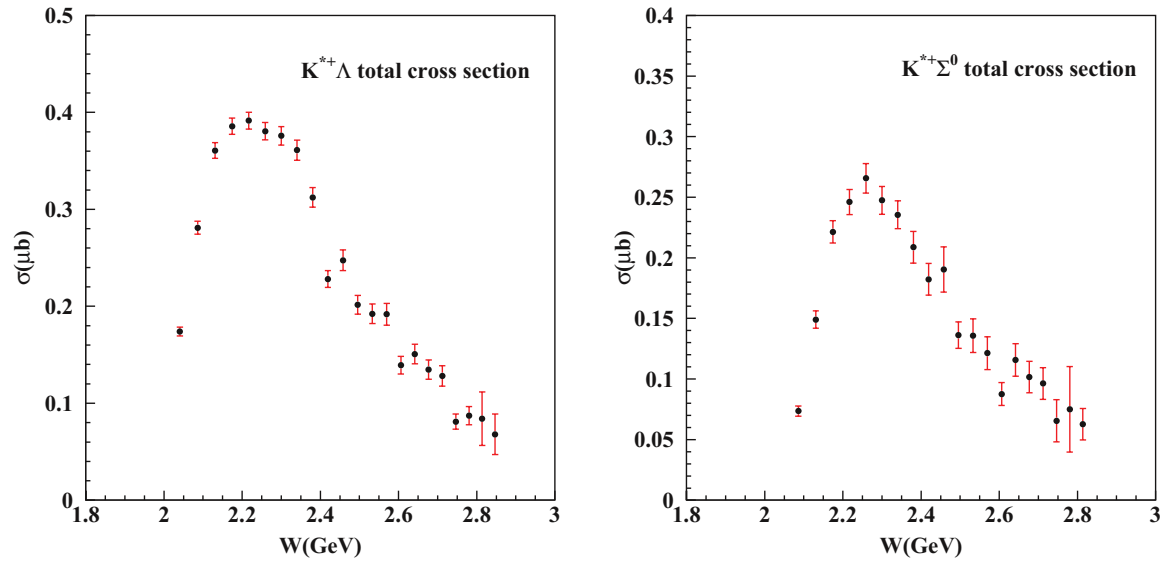

FIG. 9. (Color online) Total cross sections of the reaction $\gamma p \to K^{*+}\Lambda$ (left) and $\gamma p \to K^{*+}\Sigma^0$ (right).

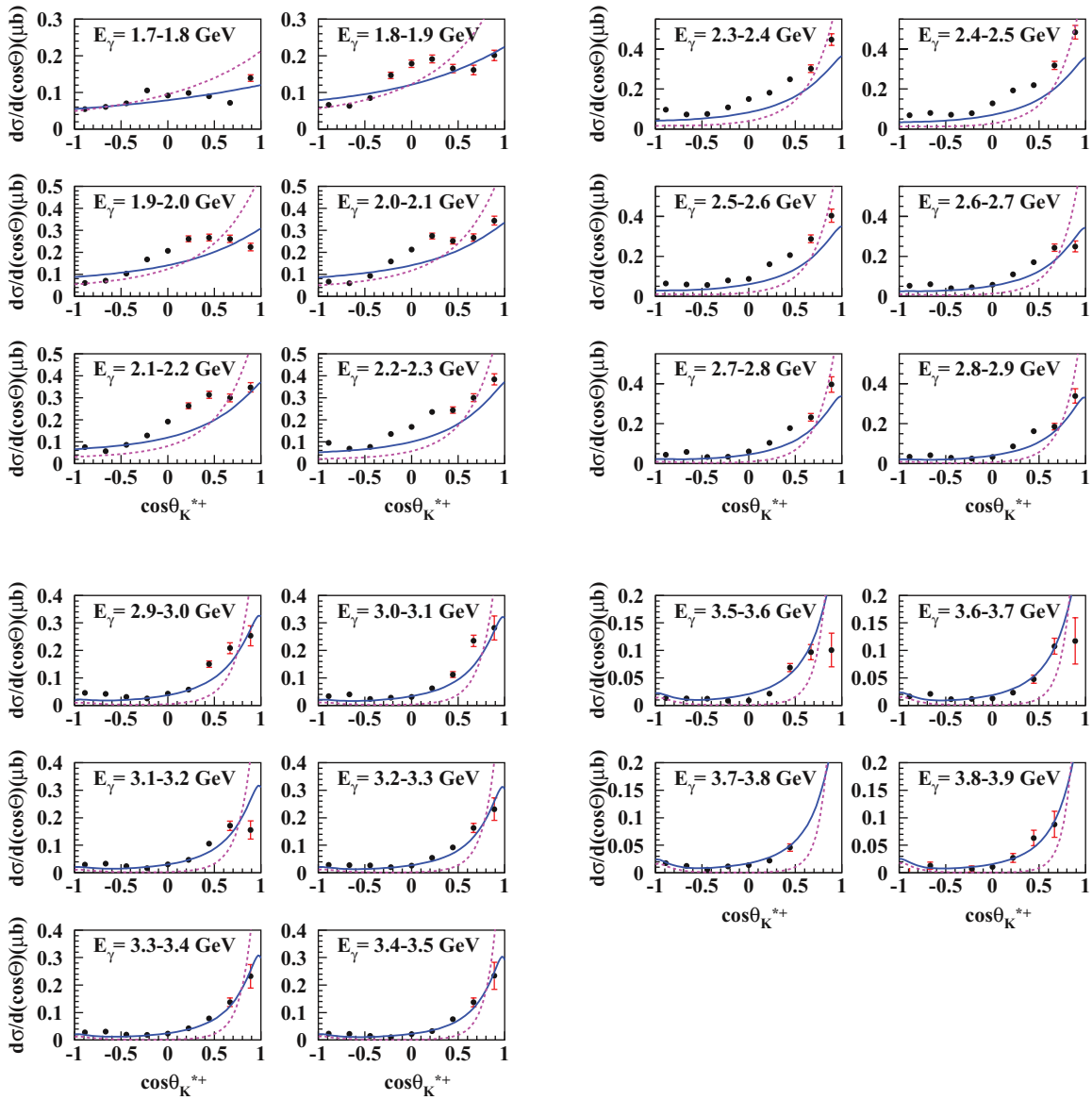

FIG. 10. (Color online) Differential cross sections of $\gamma p \to K^{*+}\Lambda$ plotted for incident photon energies from 1.7 to 3.9 GeV. The solid (blue) curves represent the theoretical calculations from the K-N-O-K model (isobar model) [20] and the dashed (magenta) curves represent the calculations of the modified O-N-H model, which is based on the O-N-H model [21] but includes two extra resonance terms [D13(2080) and D15(2200)] used in the K-N-O-K model.

the total cross section was extracted by integrating $f(x)$ over $\cos\theta$ from -1 to 1. Using the properties of the Legendre polynomials, after the integration, only the a_0 term is left. Hence the total cross section is given by $\sigma_{\text{total}} = 2a_0$.

Figure 6 shows the fitting for the $\gamma p \to K^{*+}\Lambda$ channel, and Fig. 7 shows the fits for the $K^{*+}\Sigma^0$ final state. The fitting parameters a_0 through a_4 for each channel are plotted versus the incident photon energy E_γ in Fig. 8. The extracted total cross sections are shown in Fig. 9 for the $K^{*+}\Lambda$ and $K^{*+}\Sigma^0$ final states. The error bars show only the statistical uncertainty.

A. Systematic uncertainties

Systematic uncertainties come from several sources: the applied cut parameters, the choice of fitting functions, the Monte Carlo used for the detector acceptance, and so on.

Systematic uncertainties were estimated for each cut by varying the cut intervals and then recalculating the differential cross sections. The changes to cut parameters were applied to both the experimental data and the simulated output. The relative difference between the new cross sections and the original cross sections was calculated bin by bin using

$$\delta\sigma = \frac{\sigma_{\text{new}} - \sigma_{\text{old}}}{\sigma_{\text{old}}} \tag{19}$$

and then the resulting $\delta\sigma$ values were histogrammed. This histogram was fitted with a Gaussian function, and the width from the Gaussian fit was taken as the systematic uncertainty for each variation. The cut intervals were varied to both larger and smaller values, and we chose the larger of the systematic uncertainties calculated from each variation.

TABLE II. Summary of systematic uncertainties.

	$K^{*+}\Lambda$ channel	$K^{*+}\Sigma^0$ channel
Event selections	2.9%	4.5%
Peak fitting	7.4%	5.8%
Detector acceptance	9.2%	5.7%
Beam flux	7.0%	7.0%
Other sources	2.5%	2.5%
Total	14%	12%

Similar estimation were done for the detector acceptance, by varying the inputs to the Monte Carlo. Also, different fitting functions and background shapes were used to determine the systematic uncertainties associated with the peak yields. The total systematical uncertainty is then given by

$$\delta_{\text{total}} = \sqrt{\delta_a^2 + \delta_b^2 + \delta_c^2 + \cdots} \tag{20}$$

which assumes no correlated uncertainties.

The total systematic uncertainty from all sources, added in quadrature, is shown in Table II, where the other sources include the target length, density, and so on. For the $K^{*+}\Lambda$ final state the overall systematic uncertainty is 14% and for $K^{*+}\Sigma^0$ the systematic uncertainty is 12%.

B. Theoretical calculations

The models that are currently available for K^* photoproduction are based on effective Lagrangians, which fall into two groups: isobar models and Reggeized meson exchange models. Isobar models evaluate tree-level Feynman diagrams, which include resonant and nonresonant exchanges of baryons and mesons. The Reggeized models, on the other hand, emphasize the t-channel meson exchange, which is expected to dominate the reaction at energies above the resonance region. The standard propagators in the Lagrangian are replaced by Regge propagators, which take into account an entire family of exchanged particles with the same quantum numbers (except for spin) instead of just one meson exchange. In this section, the $K^{*+}\Lambda$ cross section results will be compared with calculations from these two theoretical models.

One model we use is by Oh and Kim (O-K model) [4], which is an isobar model. This model starts with Born terms, which include t-channel (with K, K^*, and κ exchanges), s-channel ground state nucleon exchanges and u-channel Λ, Σ, and Σ^* exchanges. Additional s-channel nucleon resonance exchanges were added to the model using the known resonances from the PDG in Ref. [20], referred to here as the K-N-O-K model. One attractive point of these models is the inclusion of diagrams with a light κ meson exchange in the t channel. As mentioned in the introduction, the κ meson has not yet been firmly established, and these models allows us to study the effect of possible κ exchange.

The other model shown here is the Ozaki, Nagahiro, and Hosaka (O-N-H) model [21], which is a Reggeized model. This model takes into account all possible hadron exchanges with the same quantum numbers (except for the spin). The coupling constants and κ exchange parameters are the same as those used in the O-K model [4].

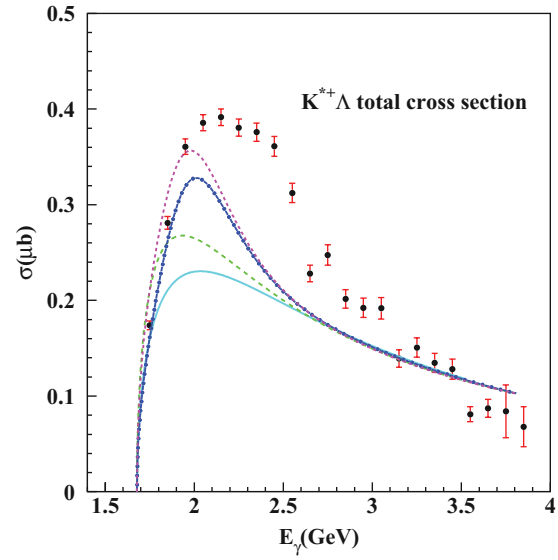

FIG. 11. (Color online) Total cross sections of the reaction $\gamma p \to K^{*+}\Lambda$. The solid (cyan) and dash-dotted (blue) curves represent the theoretical calculations from the O-K and K-N-O-K models, respectively. The dashed (green) curve represents the O-N-H model, while the dotted (magenta) curves represents the modified O-N-H model, which is based on the O-N-H model but includes two extra resonance terms used in the K-N-O-K model.

Figure 10 shows those calculations compared with our differential cross sections, where the solid curves represent the theoretical calculations from the K-N-O-K model and the dashed curves represent the O-N-H model. The corresponding curves are shown in Fig. 11 for the total cross sections, where

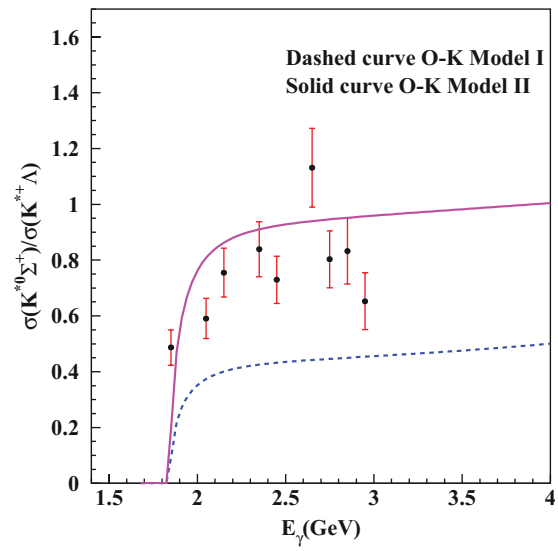

FIG. 12. (Color online) Total cross section ratio of the reactions $\gamma p \to K^{*0}\Sigma^+$ to $\gamma p \to K^{*+}\Lambda$. The ratio uses the present data in the denominator and data from Ref. [5] in the numerator. The dashed and solid curves are theoretical calculations from Oh and Kim [4] models I and II, respectively.

the curves are explained in the figure caption. The O-K model does not include any nucleon resonances, whereas the K-N-O-K model includes two s-channel resonances up to 2.2 GeV [the $D_{13}(2080)$ and $D_{15}(2200)$ resonances]. Interpretation of these results are discussed in Sec. VI.

Figure 12 shows the total cross section ratio of the reactions $\gamma p \to K^{*0}\Sigma^+$ to $\gamma p \to K^{*+}\Lambda$. The $K^{*+}\Lambda$ data alone are not very sensitive to the κ exchange due to the unknown strength of the coupling constant, $g_{\kappa N\Lambda}$. However, the coupling constants of these two reactions is related in the effective Lagrangian models, and so the ratio is sensitive to the effects of κ exchange. The dots with error bars in Fig. 12 use the present data along with the previously published CLAS data for $K^{*0}\Sigma^+$ [5]. We note that another data set exists for the $K^{*0}\Sigma^+$ reaction from CBELSA [6], but we have chosen to use CLAS data in both numerator and denominator to reduce systematics. The two curves are the theoretical predictions from O-K models I and II [4], where model I includes minimal t-channel κ exchange, while model II has a significant contribution from κ exchange.

VI. DISCUSSION AND CONCLUSIONS

We presented here the first high-statistics measurement of the reactions $\gamma p \to K^{*+}\Lambda$ and $\gamma p \to K^{*+}\Sigma^0$. The data are from the g11a experiment using the CLAS detector at Thomas Jefferson National Accelerator Facility. Differential cross sections are presented for nine equal-spaced bins in $\cos\theta^{\text{c.m.}}_{K^{*+}}$ for each photon energy bin of 0.1 GeV width from threshold (1.7 or 1.8 GeV, respectively) up to 3.9 GeV. Total cross sections, based on fits to the differential cross sections are also presented for both reactions.

The cross sections for the $K^{*+}\Lambda$ final state are compared with calculations from two effective Lagrangian models, one based on an isobar model and the other based on the Regge model. Neither calculation matches the data over the broad kinematic range measured here, but the isobar model compares more favorably, especially at higher photon energies. However, both models significantly underpredict the total cross sections in the range $2.1 < E_\gamma < 3.1$ GeV. Inclusion of two nucleon resonances improves agreement with the data in the region of $E_\gamma \sim 2$ GeV, but has only a small contribution above $\sim$2.3 GeV, and cannot explain this excess cross sections in the new data.

It remains an open question whether the excess strength of the $K^{*+}\Lambda$ final state in this photon energy region is due to additional couplings to yet-unidentified nucleon resonances at higher mass, or whether it is due to other effects such as channel-coupling through final-state interactions or interference at the amplitude level with other physics processes such as photoproduction of the $K^0\Sigma^{*+}$ final state. The latter effect was studied using a simplified Monte Carlo generator and showed little or no effect due to interference with the $K^0\Sigma^{*+}$ final state, but more sophisticated theoretical calculations should be done to study interference effects.

In comparison, the $K^{*+}\Sigma^0$ final state has a sharper peak in the total cross section at $W \sim 2.25$ GeV, and falls off more quickly with increasing photon energy than for the $K^{*+}\Lambda$ final state. This suggests whatever mechanism that causes the excess cross section for the latter final state is not present in the $K^{*+}\Sigma^0$ photoproduction. However, theoretical calculations are not yet available for this final state, and we must wait for more theoretical development before any such conclusion can be reached.

One of the goals of this measurement was to understand the role of the κ meson exchange, which can contribute to K^{*+} photoproduction but not to K^+ photoproduction. Although no definite conclusion can be reached from the present data, the ratio of total cross sections for the $K^{*+}\Lambda$ and the $K^{*0}\Sigma^+$ final state compared with a similar ratio calculated in the model of Oh and Kim suggests that the model with significant κ exchange is in better agreement with the data ratio. This agrees with the conclusion from a recent study of the beam asymmetry measurement [8] of the $K^{*0}\Sigma^+$ final state using a linearly polarized photon beam at forward angles. However, we must be careful in making any firm conclusion regarding the role of the κ exchange until the theoretical models have better agreement with the $K^{*+}\Lambda$ total cross sections above $\sim$2.1 GeV. The excess strength of the new data above 2.1 GeV may change the effects of κ exchange in the ratio. However, the general idea of comparing the $K^{*+}\Lambda$ and $K^{*0}\Sigma^+$ cross sections, which are affected differently by κ exchange, is something that can be studied now that these new data are available.

ACKNOWLEDGMENTS

The authors thank the staff of the Thomas Jefferson National Accelerator Facility who made this experiment possible. This work was supported in part by the Chilean Comisión Nacional de Investigación Científica y Tecnológica (CONICYT), the Italian Istituto Nazionale di Fisica Nucleare, the French Centre National de la Recherche Scientifique, the French Commissariat à l'Energie Atomique, the US Department of Energy, the National Science Foundation, the UK Science and Technology Facilities Council (STFC), the Scottish Universities Physics Alliance (SUPA), and the National Research Foundation of Korea. The Southeastern Universities Research Association (SURA) operates the Thomas Jefferson National Accelerator Facility for the United States Department of Energy under contract no. DE-AC05-84ER40150.

[1] J. Beringer *et al.* (Particle Data Group), Phys. Rev. D **86**, 010001 (2012).
[2] R. Machleidt, Phys. Rev. C **63**, 024001 (2001); R. Machleidt, K. Holinde, and Ch. Elster, Phys. Rep. **149**, 1 (1987).
[3] M. Ablikim *et al.*, Phys. Lett. B **633**, 681 (2006); E. M. Aitala *et al.*, Phys. Rev. Lett. **89**, 121801 (2002).
[4] Yongseok Oh and Hungchong Kim, Phys. Rev. C **74**, 015208 (2006).
[5] I. Hleiqawi *et al.* (CLAS Collaboration), Phys. Rev. C **75**, 042201(R) (2007).
[6] M. Nanova *et al.*, Eur. Phys. J. A **35**, 333 (2008).
[7] L. Guo and D. P. Weygand, arXiv:hep-ex/0601010v1.

[8] S. H. Hwang *et al.* (LEPS Collaboration), Phys. Rev. Lett. **108**, 092001 (2012).
[9] Simon Capstick and W. Roberts, Phys. Rev. D **58**, 074011 (1998).
[10] R. Bradford *et al.* (CLAS Collaboration), Phys. Rev. C **73**, 035202 (2006).
[11] A. V. Anisovich *et al.*, Eur. Phys. J. A **48**, 15 (2012); Phys. Lett. B **711**, 167 (2012).
[12] D. I. Sober *et al.*, Nucl. Instrum. Methods Phys. Res. A **440**, 263 (2000).
[13] Y. G. Sharabian *et al.*, Nucl. Instrum. Methods Phys. Res. A **556**, 246 (2006).
[14] M. D. Mestayer *et al.*, Nucl. Instrum. Methods Phys. Res. A **449**, 81 (2000).
[15] E. S. Smith *et al.*, Nucl. Instrum. Methods Phys. Res. A **432**, 265 (1999).
[16] B. A. Mecking *et al.*, Nucl. Instrum. Methods Phys. Res. A **503**, 513 (2003).
[17] Michael Williams, Ph.D. thesis, Carnegie Mellon University, 2007, http://www-meg.phys.cmu.edu/williams/pdfs/thesis.pdf.
[18] Wei Tang, Ph.D. thesis, Ohio University, 2012. https://userweb.jlab.org/∼tangwei/WeiTang_Thesis.pdf.
[19] R. De Vita *et al.* (CLAS Collaboration), Phys. Rev. D **74**, 032001 (2006).
[20] S.-H. Kim, S.-I. Nam, Y. Oh, and H.-Ch. Kim, Phys. Rev. D **84**, 114023 (2011).
[21] Sho Ozaki, Hideko Nagahiro, and Atsushi Hosaka, Phys. Rev. C **81**, 035206 (2010).